catalysts

MDPI

Article

BiOCOOH Microflowers Decorated with Ag/Ag_2CrO_4 Nanoparticles as Highly Efficient Photocatalyst for the Treatment of Toxic Wastewater

Shijie Li [1], Bing Xue [1,2], Jialin Chen [1,2], Wei Jiang [1,*] and Yanping Liu [1,2,*]

[1] Key Laboratory of Health Risk Factors for Seafood of Zhejiang Province, Institute of Innovation & Application, Zhejiang Ocean University, Zhoushan 316022, China; lishijie@zjou.edu.cn (S.L.); xb1725621827@163.com (B.X.); chenjialin_haihua@163.com (J.C.)

[2] College of Marine Science and Technology, Zhejiang Ocean University, Zhoushan 316022, China

* Correspondence: jiangwei_zjou@163.com (W.J.); liuyp@zjou.edu.cn (Y.L.); Tel.: +86-0580-67792557 (W.J.)

Received: 28 November 2019; Accepted: 5 January 2020; Published: 8 January 2020

Abstract: A novel flower-like Ag/Ag_2CrO_4/BiOCOOH heterojunction photocatalyst was synthesized by a facile in-situ precipitation strategy combined with photoreduction treatment. Morphological studies revealed that numerous Ag/Ag_2CrO_4 nanoparticles were evenly anchored on BiOCOOH microflowers, producing a novel heterojunction with the compactly interfacial contact. Optical absorption characterization demonstrated that Ag/Ag_2CrO_4/BiOCOOH possessed much better sunlight harvesting ability than Ag_2CrO_4/BiOCOOH and BiOCOOH. Photocatalytic experiments verified that compared with BiOCOOH, Ag_2CrO_4, Ag/Ag_2CrO_4, and Ag_2CrO_4/BiOCOOH, Ag/Ag_2CrO_4/BiOCOOH achieved remarkable efficiency by eliminating 100% of rhodamine B (RhB), 82.6% of methyl orange (MO) or 69.4% of ciprofloxacin (CIP) within 50 min at a catalyst dosage of 0.4 g/L. The high photocatalytic performance is likely owing to the improved sunlight response and the distinctly suppressed recombination of charge carriers arising from the formation of the novel 3D hierarchical heterostructure. The quenching test signified that h^+, and $\bullet O_2^-$ were detected as the prevailing active species in wastewater treatment. This study may provide a viable strategy for enhancing the photocatalytic performance of wide band-gap semiconductors.

Keywords: Ag/Ag_2CrO_4/BiOCOOH; ternary heterojunction; harmful pollutants; photocatalysis

1. Introduction

Semiconductor-mediated photocatalysis, an effective and environmental-friendly approach for environmental remediation, has attracted worldwide scientific interest [1–16]. Up to now, a large number of photocatalysts have been developed for environmental protection, including metals [17], organic polymers [18], sulfides [19,20], metal oxides [21–23], and nitrides [24]. In particular, BiOCOOH has stimulated tremendous interest in wastewater treatment because of its unique layer structure, low cost, high catalytic activity and chemical stability [25–28]. Nevertheless, the photocatalytic activity of pure BiOCOOH is typically quite low and primarily restrained by the inadequate sunlight absorption owing to its large band gap (Eg = ~3.7 eV), and the rapid charge recombination [25–31]. With the aim to reinforce the photocatalytic performance, a promising strategy is combining BiOCOOH with a proper semiconductor, carbon materials and/or metals to develop a multi-component heterojunction. As a result, various BiOCOOH-based binary heterojunctions (e.g., BiOCOOH/C [27], BiOCOOH/BiOCl [29], and BiOCOOH/C_3N_4 [28]), have been prepared and they all displayed better photocatalytic property compared to BiOCOOH. Recently, we have also constructed BiOCOOH/BiOBr [30], and Ag_2CO_3/BiOCOOH [31], and these heterojunctions exhibited enhanced photocatalytic behaviors. It should be noted that these BiOCOOH-based binary heterojunctions

still suffer from the unsatisfactory sunlight photoresponse and photocatalytic activity. Interestingly, the well-designed ternary heterojunction photocatalysts could be endowed with much superior photocatalytic performance than binary heterojunction photocatalysts [32]. BiOCOOH-based ternary photocatalysts are expected to possess excellent photocatalytic performances but have been rarely explored. The facile fabrication of novel BiOCOOH-based ternary photocatalysts is still a huge challenge, which is worth further researching in depth.

Silver chromate (Ag_2CrO_4, Eg = ~1.8 V) is proved a promising photosensitizer since its narrow band gap could benefit the sunlight absorption of the semiconductor photocatalysts [33–38]. More importantly, the obtained Ag/Ag_2CrO_4 through the reduction of Ag^+ to Ag^0, has been renowned as a fascinating couple to modify semiconductors for triggering robust catalytic ability because it is capable of effectively reinforcing visible-light absorption by surface plasmon resonance effect of metallic Ag and expediting the spatial separation of carriers [39]. Enlighten by the above analyses, the flowerlike heterostructure of BiOCOOH modified by Ag/Ag_2CrO_4 nanoparticles (NPs) could be anticipated to be an outstanding sunlight-driven photocatalyst for pollutant removal. However, to our knowledge, no pioneering study has been done on the exploration of Ag/Ag_2CrO_4/BiOCOOH, inspiring comprehensive research.

This research demonstrates the fabrication of an excellent heterojunction photocatalyst with Ag/Ag_2CrO_4 NPs anchored on flowerlike BiOCOOH through a facile in-situ precipitation-photoreduction strategy for the first time. The in-situ growth of Ag on Ag_2CrO_4 through photoreduction is a significant route to realize the robust bonding between Ag_2CrO_4 and Ag, which is beneficial for the efficient charge transfer. Markedly, Ag can scavenge photo-induced electrons efficiently from Ag_2CrO_4 and then migrate fast to take part in the further reaction due to its excellent conductivity. Benefiting from the novel hierarchical architecture, the Ag/Ag_2CrO_4/BiOCOOH was applied to degrade rhodamine B (RhB), ciprofloxacin (CIP) and methyl orange (MO) in aqueous solution under simulated solar light. The enhancement mechanism for the Ag/Ag_2CrO_4/BiOCOOH photocatalyst was explored.

2. Results and Discussion

2.1. Structure and Morphology

Typical XRD patterns of BiOCOOH, Ag_2CrO_4, Ag_2CrO_4/BiOCOOH, and Ag/Ag_2CrO_4/BiOCOOH are shown in Figure 1. BiOCOOH and Ag_2CrO_4 were in tetragonal structure (JCPDS 35-0939) [27,30] and orthorhombic structure (JCPDS 26-0952) [35], respectively. For Ag_2CrO_4/BiOCOOH, the diffraction peaks of BiOCOOH and Ag_2CrO_4 were detected simultaneously, verifying the successful integration of BiOCOOH and Ag_2CrO_4. As to Ag/Ag_2CrO_4/BiOCOOH, apart from the peaks from Ag_2CrO_4/BiOCOOH, one weak peak belonging to the (111) facet of cubic Ag (JCPDS No. 04-0783) was also observed, implying the successful construction of Ag/Ag_2CrO_4/BiOCOOH. Further, the decoration of Ag/Ag_2CrO_4 NPs did not change the crystalline phase of BiOCOOH, reflecting that the Ag/Ag_2CrO_4 NPs could be just deposited on the BiOCOOH rather than covalently incorporated into the crystalline phase of BiOCOOH.

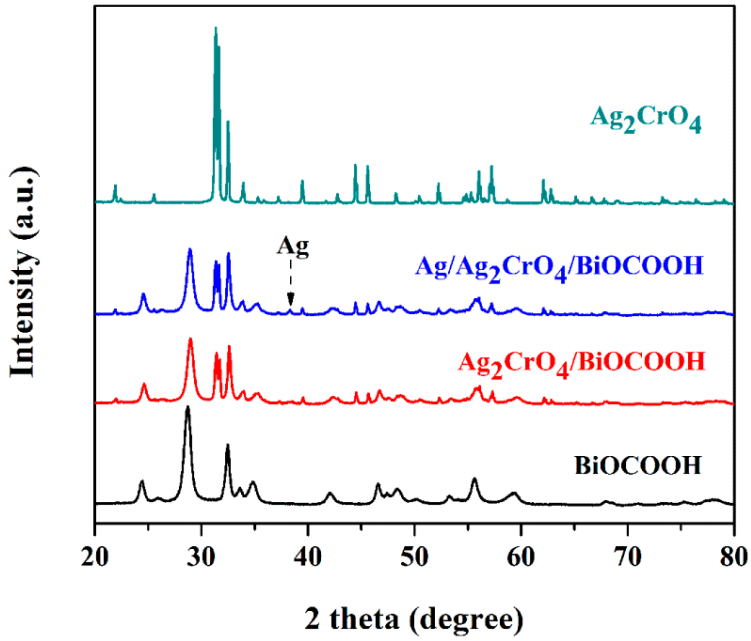

Figure 1. XRD patterns of BiOCOOH, Ag_2CrO_4 and the Ag/Ag_2CrO_4/BiOCOOH heterojunction.

The elemental constituents and valence states of Ag/Ag_2CrO_4/BiOCOOH were investigated using the X-ray photoelectron spectroscopy (XPS) (Figure 2). The full-survey XPS spectrum (Figure 2a) evidenced the co-existence of Bi, O, Ag, Cr, and C elements, in agreement with the constituents of the sample. High-resolution Bi 4f XPS spectrum (Figure 2b) showed that two peaks located at 159.2 and 164.7 eV were attributed to the Bi 4f7/2 and Bi 4f5/2 of the Bi^{3+} in BiOCOOH. As to C 1s (Figure 2c), two peaks at 284.8 and 288.1 eV corresponded to the C-OH and C-O bonding, respectively. From Figure 2d, the peaks centered at 367.8 and 373.8 eV corresponded to Ag^+ of Ag_2CrO_4, and those situated at 368.4 and 374.6 eV were associated with metallic Ag^0. This fact validated that partial Ag^+ ions were reduced to Ag^0 through irradiation. Figure 2e showed the two characteristic peaks at 578.8 and 588.1 eV, which could link to Cr $2p_{3/2}$ and Cr $2p_{1/2}$, confirming the presence of Cr^{6+} species. The peaks of O 1 s at 530.2 eV and 531.8 eV could be indexed to the lattice oxygen of Ag/Ag_2CrO_4/BiOCOOH and hydroxyl oxygen (Figure 2f). Moreover, the atomic ratio of Ag:Cr was determined to be 5.92:2.54, reflecting that the molar ratio of Ag^0:Ag_2CrO_4 was about 0.33:1. These results were in line with the XRD characterization, signifying that both BiOCOOH and Ag/Ag_2CrO_4 existed in Ag/Ag_2CrO_4/BiOCOOH.

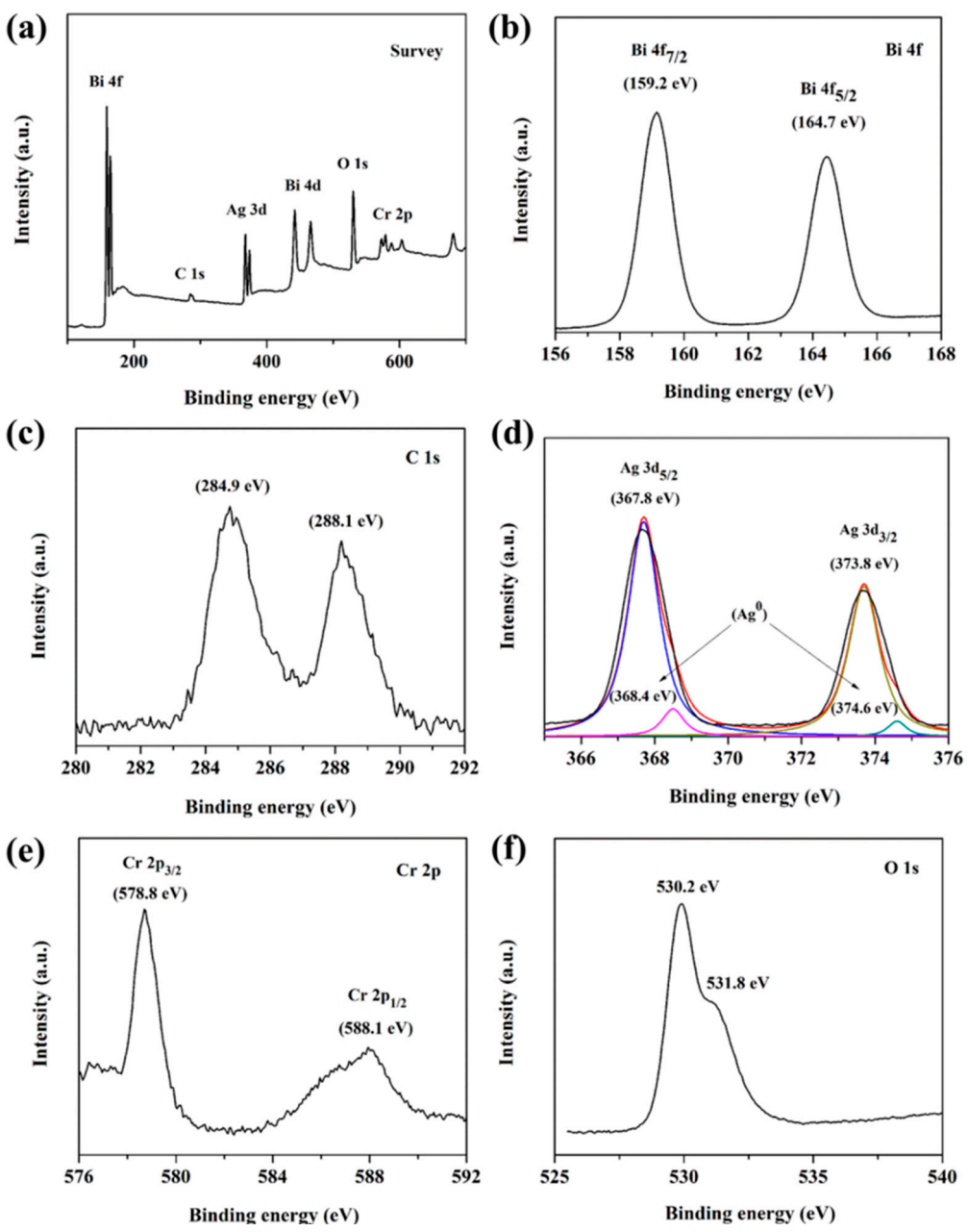

Figure 2. XPS result of Ag/Ag_2CrO_4/BiOCOOH: survey scan (**a**), Bi 4f (**b**), C 1s (**c**), Ag 3d (**d**), Cr 2p (**e**), and O 1s (**f**).

The morphologies of BiOCOOH and Ag/Ag_2CrO_4/BiOCOOH were observed based on SEM and TEM images (Figures 3 and 4). Clearly, 3D flower-like BiOCOOH (diameter: ~1.7-3 μm) microspheres were assembled by 2D nanosheets with smooth surfaces (Figure 3a,b). After its decoration with the Ag/Ag_2CrO_4 NPs, numerous Ag/Ag_2CrO_4 NPs were found on the surface of BiOCOOH microspheres (Figure 3c,d), further demonstrating the construction of the Ag/Ag_2CrO_4/BiOCOOH heterojunction. Moreover, the EDS mapping images (Figure 3c–h) reveal the even coating of Ag/Ag_2CrO_4 NPs on the BiOCOOH microsphere.

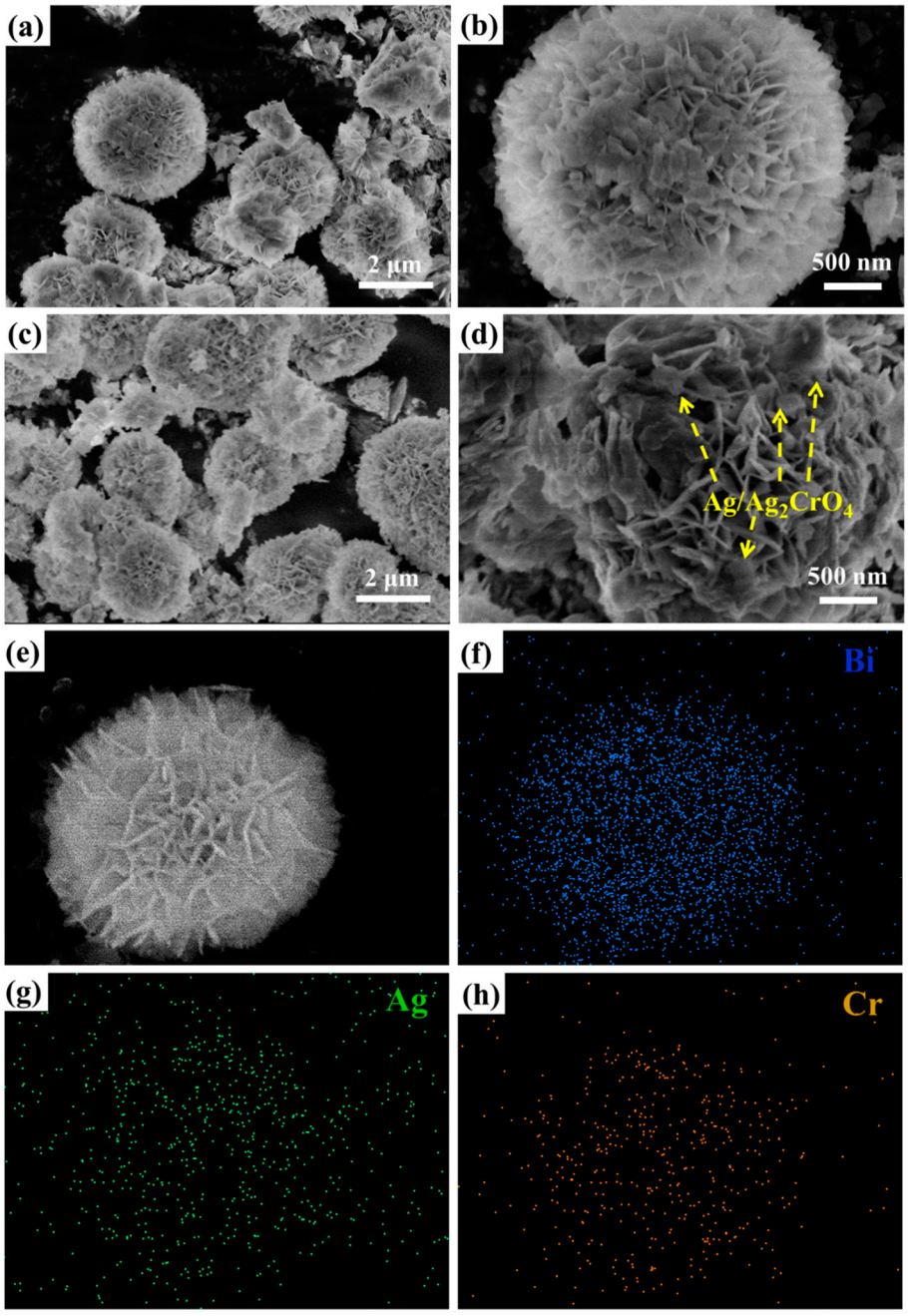

Figure 3. SEM images of bare BiOCOOH (**a**,**b**) and Ag/Ag_2CrO_4/BiOCOOH (**c**,**d**); EDS elemental mapping of Ag/Ag_2CrO_4/BiOCOOH (**e**–**h**).

The morphological features of Ag/Ag_2CrO_4/BiOCOOH were further studied by TEM. TEM images (Figure 4a,b) further reflects that the Ag/Ag_2CrO_4 NPs (size: ~20–70 nm) were intimately anchored on BiOCOOH microspheres. Of note, the in-situ deposition of Ag/Ag_2CrO_4 NPs on BiOCOOH can lead to the close contact of interfaces between them, which is conducive to the efficient separation and transformation of photo-excited carriers and therefore probably results in a prominent enhancement in the photocatalytic capability of the as-fabricated Ag/Ag_2CrO_4/BiOCOOH ternary heterojunction.

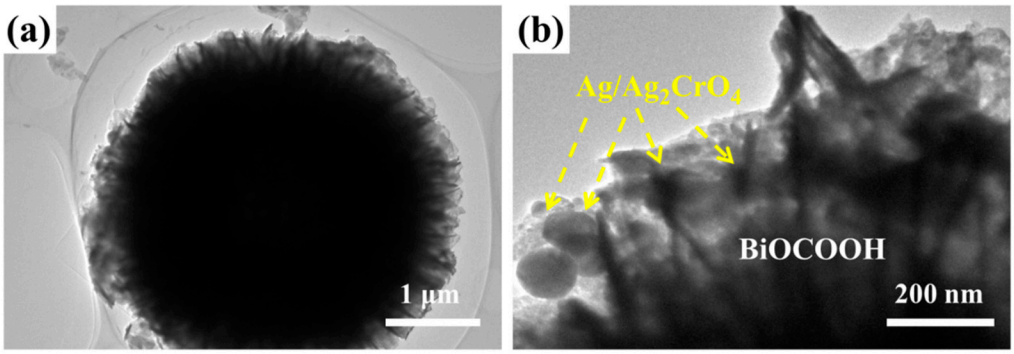

Figure 4. (**a**,**b**) TEM images of Ag/Ag_2CrO_4/BiOCOOH.

2.2. Optical Properties

UV-vis spectra of BiOCOOH, Ag_2CrO_4, and Ag/Ag_2CrO_4/BiOCOOH samples were examined to analyze the optical characteristics (Figure 5). The optical absorption verges (λ_g) of BiOCOOH and Ag_2CrO_4 are ~370 [29] and 750 nm [39], respectively. When Ag/Ag_2CrO_4 was in-situ grown on BiOCOOH, the as-prepared Ag/Ag_2CrO_4/BiOCOOH heterojunction presents a broader absorption region and stronger absorption intensity [39]. In fact, Ag NPs possess darkened color to improve the visible-light absorbance. Meanwhile, they could induce the surface plasmon resonance (SPR) absorption. This fact implies that Ag/Ag_2CrO_4/BiOCOOH could efficiently harvest solar energy for the fast elimination of pollutants.

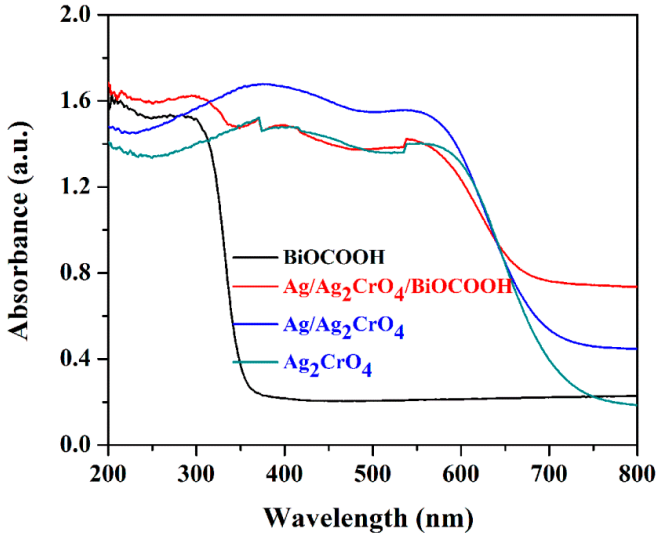

Figure 5. UV-Vis DRS of BiOCOOH, Ag_2CrO_4, Ag/Ag_2CrO_4, and Ag/Ag_2CrO_4/BiOCOOH.

Furthermore, the band gap energy (Eg) of Ag_2CrO_4 and BiOCOOH are estimated using the following equation: $\alpha h\nu = A(h\nu - Eg)^{n/2}$, where α, A, and ν are absorption coefficient, a constant and light frequency, respectively. And n equals to 4 for BiOCOOH and Ag_2CrO_4. Accordingly, the Eg of Ag_2CrO_4 and BiOCOOH can be determined to be 3.7 [26,31] and 1.8 eV [35,39] from the plot of $(\alpha h\nu)^{1/2}$ versus $h\nu$. Further, the band edge positions, namely conduction band (CB) and valence band (VB), of BiOCOOH and Ag_2CrO_4 are estimated by using the empirical equations of $E_{VB} = X - E_0 + 0.5E_g$ and $E_{CB} = E_{VB} - E_g$, consequently, the CB and VB potentials (E_{CB}) of BiOCOOH are −0.67 and 2.73 eV (versus NHE), respectively, while those of Ag_2CrO_4 are 0.47 and 2.27 eV (versus NHE), respectively.

2.3. Photocatalytic Activity

To demonstrate the potential application of the as-prepared samples, the photocatalytic degradation of RhB was first performed under simulated solar illumination (Figure S1 and Figure 6). Prior to photocatalytic reactions, all the as-fabricated photocatalysts were vigorously stirred for 1h to realize saturation adsorption (Figure S1). Apparently, BiOCOOH possessed a relatively stronger ability to adsorb RhB compared to other samples. After 60 min in the dark, 21.2% of RhB was adsorpted by BiOCOOH (Figure S1). RhB is stable and nearly no photolysis of RhB happened after 50 min of simulated solar irradiation. When employing BiOCOOH, Ag_2CrO_4, Ag_2CrO_4/BiOCOOH, or Ag/Ag_2CrO_4/BiOCOOH as the photocatalyst, after illumination for 50 min, about 25.7%, 41.3%, 50.9%, 78.3% or 100% of RhB was photo-catalytically eliminated. Clearly, Ag/Ag_2CrO_4/BiOCOOH presented the best catalytic capability for degrading RhB (Figure 6a). Furthermore, the photocatalytic capability was superior to the previously reported BiOCOOH-based samples (e.g., Ag_2CO_3/BiOCOOH [31] and BiOBr/BiOCOOH [30]) due to the formation of BiOCOOH-based three-component heterojunction (Table 1). Moreover, the BET surface areas of BiOCOOH, Ag_2CrO_4/BiOCOOH, and Ag/Ag_2CrO_4/BiOCOOH were determined as 27.35, 25.76, and 25.11 m^2g^{-1}, respectively (Table S1). Clearly, the BET surface area of Ag/Ag_2CrO_4/BiOCOOH is not the largest. This fact demonstrates that the decisive role of Ag/Ag_2CrO_4 rather than the BET surface area in enhancing the photocatalytic activity of Ag/Ag_2CrO_4/BiOCOOH. Of note, the degradation efficiency of RhB by Ag/Ag_2CrO_4/BiOCOOH was substantially improved relative to a mechanical mixture of Ag/Ag_2CrO_4 and BiOCOOH (59.6%), which might be ascribed to the effective separation of photo-induced carriers at the heterojunction interface between Ag/Ag_2CrO_4 and BiOCOOH (Figure 6a).

Table 1. The photocatalytic degradation parameters by different BiOCOOH-based photocatalysts.

Photocatalysts	Light	Photocatalytic Activity	Ref
Ag_2CO_3/BiOCOOH (ACO/BOCH-30)	300W-Xe lamp	The RhB removal efficiency reach 89.4% within 60 min over 30 mg of catalysts	[29]
BiOBr/BiOCOOH (0.6Br-Bi)	300W-Xe lamp	The RhB removal efficiency reach 100% within 50 min over 50 mg of catalysts	[28]
Ag/Ag_2CrO_4/BiOCOOH	300W-Xe lamp	The RhB removal efficiency reach 100% within 50 min over 40 mg of catalysts	This work

Figure 6b shows the apparent photo-degradation rate constants (k) for as-prepared samples. Apparently, Ag/Ag_2CrO_4/BiOCOOH achieved the largest k value of 0.0870 min^{-1}, which was pronouncedly greater than that of BiOCOOH (0.0052 min^{-1}), Ag_2CrO_4 (0.0101 min^{-1}), Ag_2CrO_4/BiOCOOH (0.0300 min^{-1}), or Ag/Ag_2CrO_4 (0.0146 min^{-1}).

Besides, to further explore the mineralization index of RhB over BiOCOOH, Ag/Ag_2CrO_4, Ag_2CrO_4/BiOCOOH, and Ag/Ag_2CrO_4/BiOCOOH during the photocatalytic reaction, the total organic carbon (TOC) values were measured and analyzed. As presented in Figure 6c, 42.3%, 27.8%, 12.4%, and 14.9% TOC decrease were observed by using Ag/Ag_2CrO_4/BiOCOOH, Ag_2CrO_4/BiOCOOH, BiOCOOH, and Ag/Ag_2CrO_4, respectively. Apparently, Ag/Ag_2CrO_4/BiOCOOH owned the highest mineralization efficiency for RhB degradation among these samples.

The photochemical stability is also a crucial parameter in industrial applications [24,40,41]. Figure 6d displays the cycling performance of Ag/Ag_2CrO_4/BiOCOOH. Ag/Ag_2CrO_4/BiOCOOH has no dramatic decline in the photodegradation behavior of RhB during five successive runs. Besides, the Ag+ leaching after the photocatalytic reaction was investigated and the leaching quantity of the Ag ion was tested to be 0.013 ppm. Further, there is no distinct change in its crystalline phases and microstructures through the analysis of the XRD pattern and TEM image of the Ag/Ag_2CrO_4/BiOCOOH heterojunction after the recycling runs (Figure 7 and Figure S2), verifying the superior stability of Ag/Ag_2CrO_4/BiOCOOH.

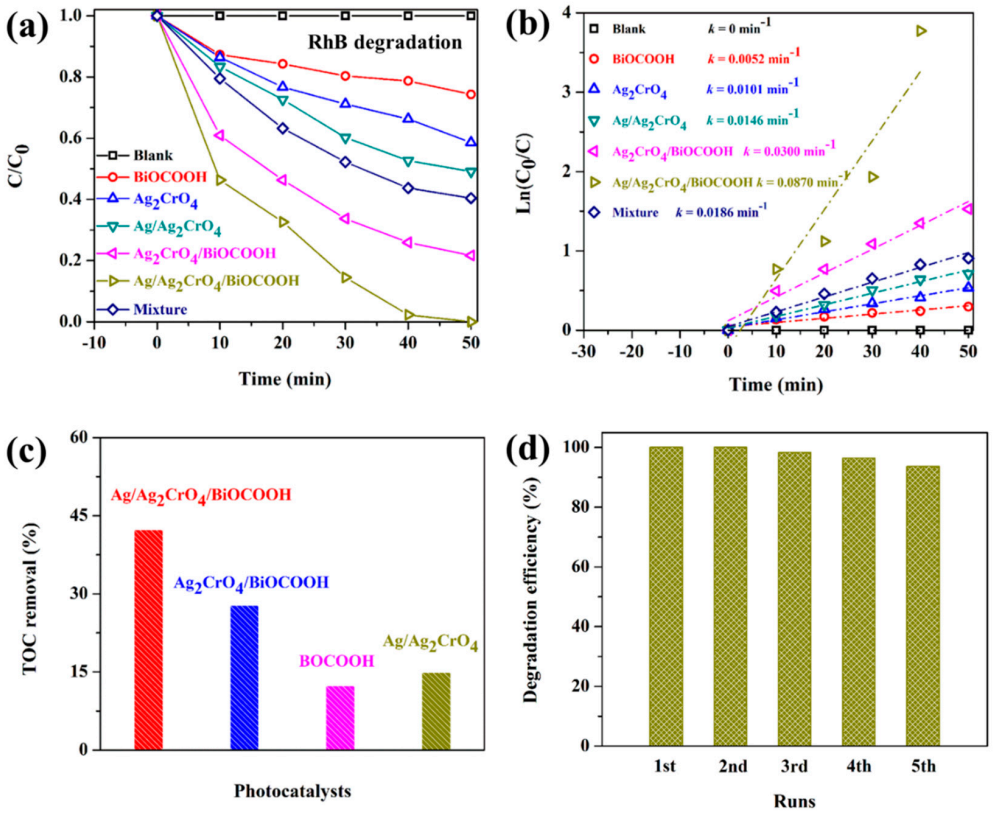

Figure 6. (**a**,**b**) Photocatalytic elimination of RhB (10 mg/L, 100 mL) aqueous solution over various samples (40 mg) under simulated solar light; (**c**) TOC removal of RhB (10 mg/L, 100 mL) aqueous solution over BiOCOOH, Ag/Ag_2CrO_4, Ag_2CrO_4/BiOCOOH and Ag/Ag_2CrO_4/BiOCOOH within 50 min of reaction. (**d**) Cycling test of Ag/Ag_2CrO_4/BiOCOOH for RhB degradation.

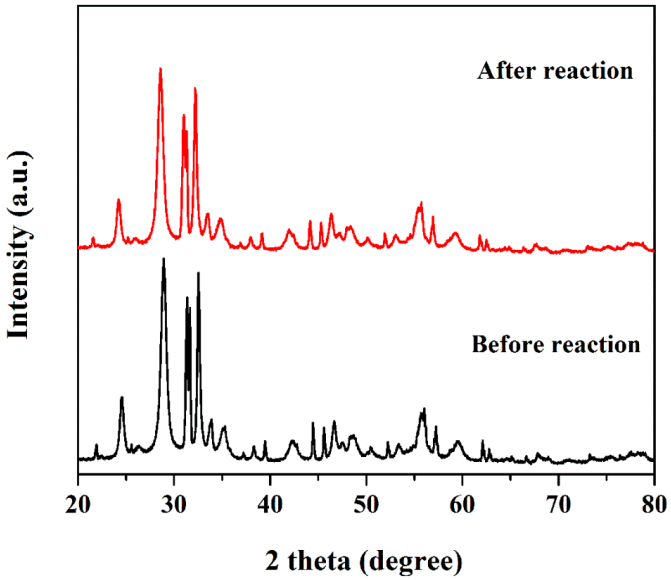

Figure 7. XRD patterns of Ag/Ag_2CrO_4/BiOCOOH before and after cycling tests.

In addition, industrial dye MO and antibiotic CIP were chosen as the model pollutants to further manifest the remarkable photocatalytic activity of Ag/Ag_2CrO_4/BiOCOOH. As shown in Figure 8, 82.6% of MO and 69.4% of CIP can be efficiently eliminated within 50 min of simulated sunlight irradiation. Therefore, it can be inferred that Ag/Ag_2CrO_4/BiOCOOH possesses the superior degradation ability for industrial dyes (RhB and MO) and antibiotic (CIP).

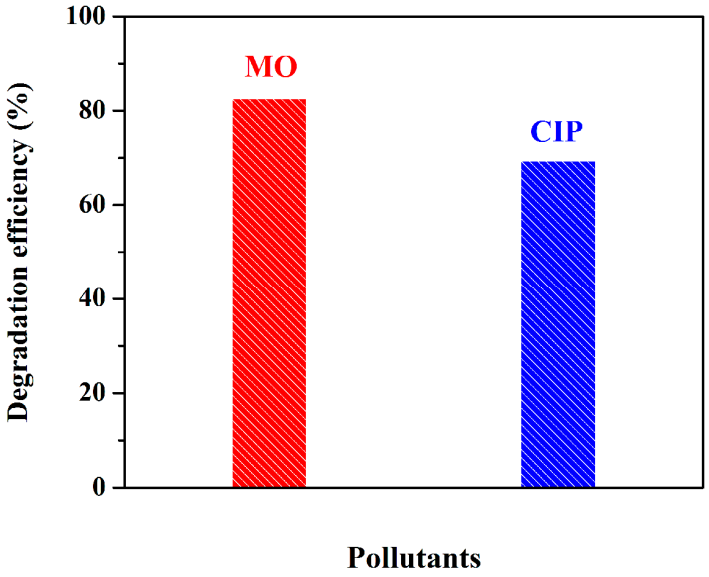

Figure 8. Photo-degradation efficiencies of MO (10 mg/L, 100 mL) and CIP (10 mg/L, 100 mL) aqueous solutions over $Ag/Ag_2CrO_4/BiOCOOH$ within 50 min of simulated solar irradiation.

2.4. Photocatalytic Mechanism

In order to speculate the mechanism of photocatalytic decomposition of contaminants over the $Ag/Ag_2CrO_4/BiOCOOH$, the exact effects of probably generated reactive species on the photo-degradation of RhB was investigated by the radical quenching experiment. 1 mM of ammonium oxalate (AO), isopropyl alcohol (IPA), or benzoquinone (BQ) was adopted to consume h^+, •OH, or $O_2^{\bullet-}$ species during the photocatalytic reaction. From Figure 9, upon the addition of AO and BQ into the photocatalytic system, the elimination efficiency of RhB distinctly decreased from 100% to 43.4% and 23.2%, respectively, evidencing the premier role of h^+ and $\bullet O_2^-$ in RhB removal. However, IPA exerts little influence on the RhB degradation, implying the subordinate role of •OH radicals.

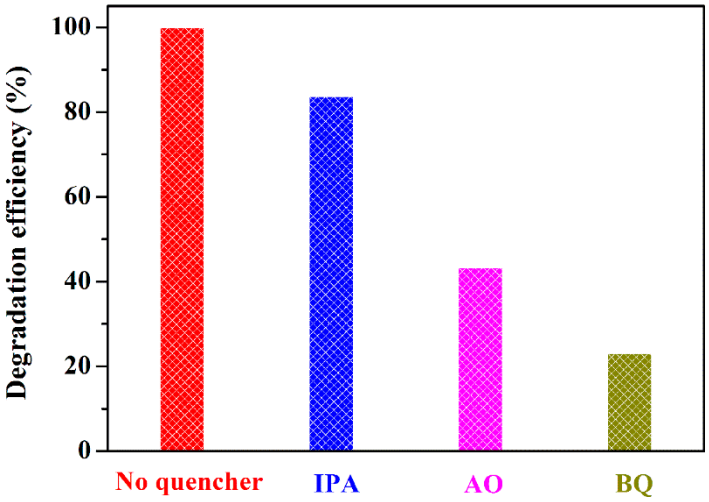

Figure 9. Impacts of various quenching agents on the photocatalytic activity of $Ag/Ag_2CrO_4/BiOCOOH$.

Photoluminescence (PL) spectroscopy was adopted to investigate the charge separation rate, which plays an essential role in determining the photocatalytic capability of a photocatalyst [41–43]. Generally, a weakened PL signal corroborates an improvement in separation efficiency of photo-induced carriers [22,29,30,41,42,44]. As exhibited in Figure 10, compared with bare BiOCOOH, $Ag/Ag_2CrO_4/BiOCOOH$ emerges with a distinctly lower emission intensity, demonstrating the

remarkable improvement of charge separation efficiency for $Ag/Ag_2CrO_4/BiOCOOH$. Thus, it can be inferred that the construction of $Ag/Ag_2CrO_4/BiOCOOH$ ternary heterojunction can effectively impede the reunion of carriers, probably leading to a superior photocatalytic activity.

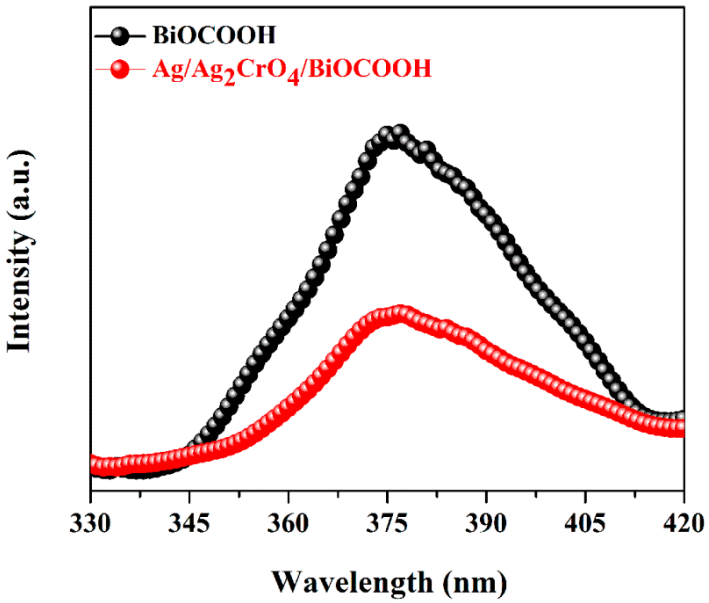

Figure 10. PL spectra of BiOCOOH, and $Ag/Ag_2CrO_4/BiOCOOH$.

On account of the above characterization and analysis, a probable mechanism for the drastically elevated photocatalytic ability of $Ag/Ag_2CrO_4/BiOCOOH$ is put forward (Figure 11). The remarkable photocatalytic activity of $Ag/Ag_2CrO_4/BiOCOOH$ principally arises from the novel hierarchical heterostructure, which achieves an appreciable improvement of light absorption (Figure 5) and carrier separation (Figure 10) [2,45–48]. Upon simulated solar illumination, both BiOCOOH and Ag_2CrO_4 are excited to trigger the production of electrons and holes on the corresponding CB and VB, respectively. Both the CB and VB potentials of Ag_2CrO_4 are lower than those of BiOCOOH. Hence, partial photo-induced electrons from the CB of BiOCOOH can preferably drift into that of Ag_2CrO_4, and then the accumulated electrons rapidly flow into the metallic Ag NPs that act as electron scavenging centers [39]. Simultaneously, part of photo-induced electrons the CB of BiOCOOH are involved in the reduction of O_2 to yield $\bullet O_2^-$ since the CB potential of BiOCOOH is more negative than the $\varphi(O2/\bullet O_2^-)$ (−0.33 eV versus NHE). This result is in good agreement with that of the trapping experiments (Figure 9). On the other hand, the photo-induced holes on the VB of BiOCOOH are injected into that of Ag_2CrO_4. Such carrier movement makes charge separation more effective, which is beneficial for the efficient production of reactive species [49]. Under the circumstances, enriched holes on the VB of Ag_2CrO_4 and plenty of $O_2^{\bullet -}$ radicals are engaged in the elimination of RhB and CIP. The radical quenching experiment has also verified that h^+ and $\bullet O_2^-$, not •OH radicals, principally accounts for the photocatalytic destruction of contaminants (Figure 9). In a word, such a novel hierarchical heterostructure not only could appreciably facilitate the separation of photo-excited holes and electrons but also pronouncedly ameliorate the optical absorption to realize the efficient decomposition and mineralization of harmful contaminants under simulated solar light.

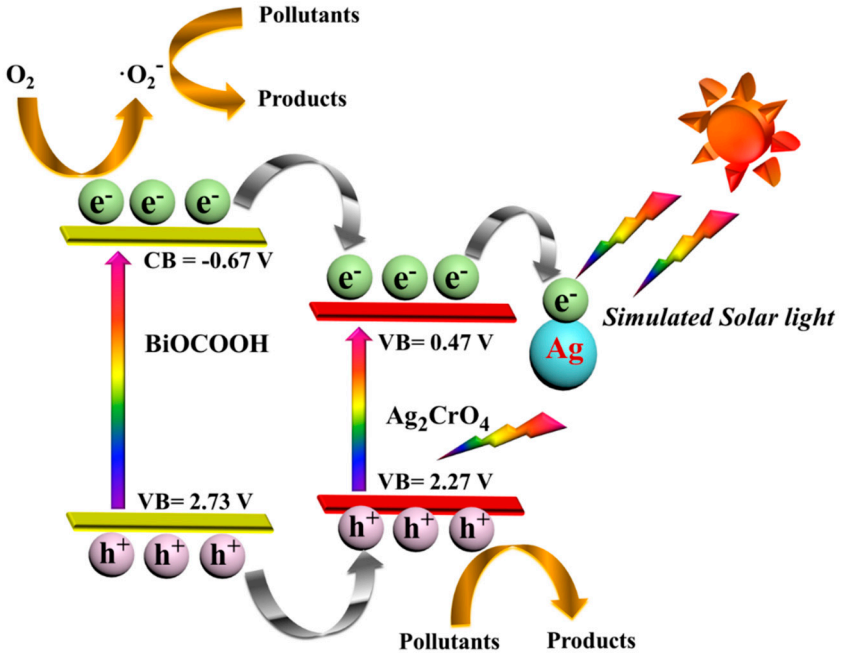

Figure 11. The proposed photocatalysis mechanism of $Ag/Ag_2CrO_4/BiOCOOH$ under simulated solar light.

3. Materials and Methods

3.1. Chemicals

All reagents of analytical grade were obtained from Chinese Sinopharm.

3.2. Photocatalysts Fabrication

BiOCOOH was fabricated basing on a reported route [30,50]. Typically, 0.96 g of $Bi(NO_3)_3{\cdot}5H_2O$ was taken into 50 mL of glycerol and sonicated for 15 min, followed by the addition of 20 mL of DMF and 10 mL of deionized water under vigorously stirring. The stirring further lasted for 60 min. After that, the solution was transferred into an autoclave heated at 160 °C for 20 h in an electric oven, and subsequently cooled down naturally. The BiOCOOH sample was washed three times, and then dried at 70 °C overnight. $Ag_2CrO_4/BiOCOOH$ was constructed via a simple in-situ deposition route. First, 3 mmol of BiOCOOH was uniformly dispersed in 100 mL of H_2O via ultra-sonication treatment. Then, 1 mmol of $AgNO_3$ and 0.2 g of Polyvinylpyrrolidone (PVP, Mw = 40,000) were added to the above solution to form solution A, followed by vigorously stirring at a stirring speed of 1000 rpm (Revolutions Per minute) for 1 h. After that, 0.5 mmol of K_2CrO_4 was ultrasonically dissolved in 10 mL of H_2O to form solution B. Afterward, solution B was dropwise added into solution A by using a syringe pump at a speed of 5 mL/h under constant stirring (1000 r/min). The resultant solution was further stirred for another 2 h. Finally, the $Ag_2CrO_4/BiOCOOH$ sample was rinsed more than four times and then dried at 70 °C overnight. The $Ag_2CrO_4/BiOCOOH$ sample was collected by centrifugation (5000 r/min) for 5 min, washed thoroughly with water five times, and dried at 70 °C overnight. $Ag/Ag_2CrO_4/BiOCOOH$ was fabricated via the photo-reduction of $Ag_2CrO_4/BiOCOOH$. Typically, 0.3 g of $Ag_2CrO_4/BiOCOOH$ was mixed with the solution of 40 mL H_2O and 20 mL methanol under stirring for half an hour. Afterwards, the suspension was irradiated by the light (Light intensity = ~170 mW/cm^2; The distance between the Xe lamp and the top of the suspension = ~25 cm.) from a 300 W Xe lamp for 2 h with constant agitation. Lastly, the as-fabricated $Ag/Ag_2CrO_4/BiOCOOH$ was collected after centrifugation (5000 r/min) for 5 min.

3.3. Characterization

The details about characterization methods are supplied in the Supporting Information (Experimental Section).

3.4. Photocatalytic Activity Evaluation

The application of $Ag/Ag_2CrO_4/BiOCOOH$ to the elimination of RhB (10 mg/L, 100 mL) or CIP (10 mg/L, 100 mL) was evaluated under simulated solar light by utilizing a 300 W Xe lamp (CEL-PF300, Beijing China Education Au-light Co., Ltd., Beijing, China) without any light filter as the simulated solar light source [51]. The light intensity was determined as ~170 mW/cm^2. The distance between the Xe lamp and the top of the reactor mouth was about 20 cm. The temperature of the photocatalytic system was maintained at about 22 °C. Typically, 40 mg of photocatalyst and 100 mL of RhB (10 mg/L), CIP (10 mg/L) or MO (10 mg/L) were mixed in a reactor under magnetically stirring (800 r/min) in the dark for 1 h to reach adsorptive equilibrium. During the photocatalytic reaction, a small portion of the solution (2 mL) was drawn every 10 min and subsequently centrifuged (speed: 9000 r/min) for 6 min to get rid of the catalysts. The obtained supernatant was analyzed using a UV-vis spectrophotometer (Shimadzu UV-2600, Tokyo, Japan) at the corresponding maximum absorption wavelength (554 nm for RhB, 276 nm for CIP, 464 nm for MO). The degradation efficiency (η) of RhB, CIP or MO was calculated by using the equation: $\eta = C_t/C_0 \times 100\%$, here C_0 and C_t are the absorbance of the contaminant solution after 1 h of stirring in dark and the absorbance of the contaminant solution at time t, respectively. The stability of $Ag/Ag_2CrO_4/BiOCOOH$ was tested for five consecutive runs. After each round, the photocatalyst was collected, centrifuged, washed with water, and subsequently dried at 60 °C overnight. After that, the photocatalyst was subjected to the next run. Due to the inevitable loss of photocatalysts during the recycling process, some parallel tests were carried out to guarantee that the dosage of photocatalyst utilized in each round was the same (40 mg). Total organic carbon (TOC) of RhB solutions during the reaction was monitored by using a Shimadzu TOC–LCSH/CPH analyzer (Shimadzu TOC–LCSH/CPH, Tokyo, Japan).

4. Conclusions

We have developed an efficient photocatalytic system of a novel 3D flower-like $Ag/Ag_2CrO_4/BiOCOOH$ heterojunction by a facile in-situ route. Such a hierarchical heterostructure not only could remarkably boost the separation of photo-excited holes and electrons but also pronouncedly strengthen the sunlight absorption to realize the efficient utilization of solar light. Compared to BiOCOOH, Ag_2CrO_4, Ag/Ag_2CrO_4, and $Ag_2CrO_4/BiOCOOH$, $Ag/Ag_2CrO_4/BiOCOOH$ exhibits a remarkable enhancement in photocatalytic elimination of harmful pollutants under simulated solar irradiation. The premier role of Ag/Ag_2CrO_4 for the upgrading the photocatalytic capability could endow $Ag/Ag_2CrO_4/BiOCOOH$ with sufficient light absorption and efficient separation of carriers. The h^+ and $\bullet O_2^-$ radicals predominantly account for the destruction of contaminants. Further, $Ag/Ag_2CrO_4/BiOCOOH$ has high stability and powerful mineralizing ability, making it favorable for real wastewater treatment. This study offers a simple route for improving the photocatalytic performance of the wide band-gap semiconductor photocatalysts and constructing a highly efficient hierarchical heterojunction for environmental remediation.

Supplementary Materials: The following are available online at http://www.mdpi.com/2073-4344/10/1/93/s1. Supplementary data associated with this article can be found, in the online version, Experimental Section: The details about characterization methods.

Author Contributions: Conceptualization, S.L.; Formal analysis, Y.L.; Investigation, S.L.; Project administration, B.X. and J.C.; Resources, W.J.; Writing—original draft, S.L. All authors have read and agreed to the published version of the manuscript.

Funding: This work has been financially supported by the Fundamental Research Funds for Zhejiang Provincial Universities and Research Institutes (2019JZ00009), the National Natural Science Foundation of China (51708504;

U1809214), the Public Projects of Zhejiang Province (LGN18E080003), and the Natural Science Foundation of Zhejiang Province (LY20E080014), the Science and Technology Project of Zhoushan (2017C41006, 2020C43001).

Conflicts of Interest: The authors declare no conflict of interest.

References

1. Zhang, L.; Lin, C.; Zhang, D.; Gong, L.; Zhu, Y.; Xu, Q.; Li, H.; Xia, Z. Guiding principles for designing highly efficient metal-free carbon catalysts. *Adv. Mater.* **2019**, *31*, 1805252. [CrossRef]
2. Xin, X.; Li, S.-H.; Zhang, N.; Tang, Z.-R.; Xu, Y.-J. 3D graphene/AgBr/Ag cascade aerogel for efficient photocatalytic disinfection. *Appl. Catal. B* **2019**, *245*, 343–350. [CrossRef]
3. Wang, R.; Li, D.; Wang, H.; Liu, C.; Xu, L. Preparation, characterization, and performance analysis of S-doped Bi_2MoO_6 nanosheets. *Nanomaterials* **2019**, *9*, 1341. [CrossRef]
4. Li, P.; Li, J.; Feng, X.; Li, J.; Hao, Y.; Zhang, J.; Wang, H.; Yin, A.; Zhou, J.; Ma, X.; et al. Metal-organic frameworks with photocatalytic bactericidal activity for integrated air cleaning. *Nat. Commun.* **2019**, *10*, 2177. [CrossRef] [PubMed]
5. Xie, X.; Zhang, N.; Tang, Z.-R.; Xu, Y.-J. Adaptive geometry regulation strategy for 3D graphene materials: Towards advanced hybrid photocatalysts. *Chem. Sci.* **2018**, *9*, 8876–8882. [CrossRef] [PubMed]
6. Kong, L.; Ambrosi, A.; Zafir, M.; Guan, J.; Pumera, M. Smart robots: Self-propelled 3D-printed "Aircraft Carrier" of light-powered smart micromachines for large-volume nitroaromatic explosives removal. *Adv. Funct. Mater.* **2019**, *29*, 190387.
7. Li, S.; Shen, X.; Liu, J.; Zhang, L. Synthesis of Ta_3N_5/Bi_2MoO_6 core-shell fiber-shaped heterojunctions as efficient and easily recyclable photocatalysts. *Environ. Sci. Nano* **2017**, *4*, 1155–1167. [CrossRef]
8. Li, S.; Hu, S.; Jiang, W.; Liu, Y.; Zhou, Y.; Liu, Y.; Mo, L. Hierarchical architectures of bismuth molybdate nanosheets onto nickel titanate nanofibers: Facile synthesis and efficient photocatalytic removal of tetracycline hydrochloride. *J. Colloid Interface Sci.* **2018**, *521*, 42–49. [CrossRef]
9. Pirhashemi, M.; Habibi-Yangjeh, A.; Pouran, S.R. Review on the criteria anticipated for the fabrication of highly efficient ZnO-based visible-light-driven photocatalysts. *J. Ind. Eng. Chem.* **2018**, *62*, 1–25. [CrossRef]
10. Simeonidis, K.; Mourdikoudis, S.; Kaprara, E.; Mitrakas, M.; Polavarapu, L. Inorganic engineered nanoparticles in drinking water treatment: A critical review. *Environ. Sci. Water Res. Technol.* **2016**, *2*, 43–70. [CrossRef]
11. Zhu, L.; Tian, Y.; Li, M.; Ma, H.; Ma, C.; Dong, X.; Zhang, X. Fabrication and photo-electrocatalytic activity of black TiO_2 embedded Ti/PbO_2 electrode. *J. Appl. Electrochem.* **2017**, *47*, 1045–1056. [CrossRef]
12. Zhao, M.; Fu, Y.; Ma, H.; Ma, C.; Dong, X.; Zhang, X. Synthesis, characterization and photoreactivity of hierarchically N-doped $(BiO)_2CO_3/Bi_2S_3$ with highly exposed {001} facets. *Mater. Des.* **2016**, *93*, 1–8. [CrossRef]
13. Zhang, C.; Li, Y.; Shuai, D.; Shen, Y.; Wang, D. Progress and challenges in photocatalytic disinfection of waterborne Viruses: A review to fill current knowledge gaps. *Chem. Eng. J.* **2019**, *335*, 399–415. [CrossRef]
14. Jiang, Z.J.; Sun, H.; Wang, T.; Wang, B.; Wei, W.; Li, H.; Yuan, S.; An, T.; Zhao, H.; Yu, J.; et al. Nature-inspired catalyst for visible-light-driven photocatalytic CO_2 reduction. *Energy Environ. Sci.* **2018**, *11*, 2382–2389. [CrossRef]
15. Li, S.; Chen, J.; Hu, S.; Jiang, W.; Liu, Y.; Liu, J. A novel 3D Z-scheme heterojunction photocatalyst: $Ag_6Si_2O_7$ anchored on flower-like Bi_2WO_6 and its excellent photocatalytic performance for the degradation of toxic pharmaceutical antibiotics. *Inorg. Chem. Front.* **2020**. [CrossRef]
16. Lee, S.H.; Lee, K.-S.; Sorcar, S.; Razzaq, A.; Grimesc, C.A.; In, S.-I. Wastewater treatment and electricity generation from a sunlight-powered single chamber microbial fuel cell. *J. Photochem. Photobiol. A Chem.* **2018**, *358*, 432–440. [CrossRef]
17. Han, N.; Wang, Y.; Yang, H.; Deng, J.; Wu, J.; Li, Y.; Li, Y. Ultrathin bismuth nanosheets from in situ topotactic transformation for selective electrocatalytic CO_2 reduction to formate. *Nat. Commun.* **2019**, *9*, 1320. [CrossRef]
18. Zhang, G.; Lin, L.; Li, G.; Zhang, Y.; Savateev, A.; Zafeiratos, S.; Wang, X.; Antonietti, M. Ionothermal Synthesis of Triazine-Heptazine Based Co-frameworks with Apparent Quantum Yields of 60% at 420 nm for Solar Hydrogen Production from "Sea Water". *Angew. Chem. Int. Ed.* **2018**, *57*, 9372–9376. [CrossRef]
19. Qiming, S.; Wang, N.; Yu, J.; Yu, J.C. A hollow porous CdS photocatalyst. *Adv. Mater.* **2018**, *30*, 1804368.

20. She, H.; Sun, Y.; Li, S.; Wang, Q. Synthesis of Non-noble Metal Nickel Doped Sulfide Solid Solution for Improved Photocatalytic Performance. *Appl. Catal. B* **2019**, *245*, 439–447. [CrossRef]
21. Xu, B.; An, Y.; Liu, Y.; Qin, X.; Zhang, X.; Dai, Y.; Wang, Z.; Wang, P.; Whangbo, M.-H.; Huang, B. Enhancing the photocatalytic activity of BiOX (X = Cl, Br, I), $(BiO)_2CO_3$ and Bi_2O_3 by modifying their surfaces with polar organic anions, 4-substituted thiophenolates. *J. Mater. Chem. A* **2017**, *5*, 14406–14414. [CrossRef]
22. Li, S.; Hu, S.; Jiang, W.; Zhou, Y.; Liu, J.; Wang, Z. Facile synthesis of cerium oxide nanoparticles decorated flower-like bismuth molybdate for enhanced photocatalytic activity toward organic pollutant degradation. *J. Colloid Interface Sci.* **2018**, *530*, 171–178. [CrossRef] [PubMed]
23. Cerrato, E.; Gionco, C.; Paganini, M.C.; Giamello, E.; Albanese, E.; Pacchioni, G. Origin of Visible Light Photoactivity of the CeO_2/ZnO Heterojunction. *ACS Appl. Energy Mater.* **2018**, *1*, 4247–4260. [CrossRef]
24. Pei, L.; Yuan, Y.; Zhong, J.; Li, T.; Yang, T.; Yan, S.; Ji, Z.; Zou, Z. Ta_3N_5 nanorods encapsulated into 3D hydrangea-like MoS_2 for enhanced photocatalytic hydrogen evolution under visible light irradiation. *Dalton Trans.* **2019**, *48*, 13176–13183. [CrossRef] [PubMed]
25. Yang, L.L.; Han, Q.F.; Wang, X.; Zhu, J.W. Highly efficient removal of aqueous chromate and organic dyes by ultralong HCOOBiO nanowires. *Chem. Eng. J.* **2015**, *262*, 169–178. [CrossRef]
26. Xiong, J.Y.; Cheng, G.; Lu, Z.; Tang, J.L.; Yu, X.L.; Chen, R. BiOCOOH hierarchical nanostructures: Shape-controlled solvothermal synthesis and photocatalytic degradation performances. *CrystEngComm* **2011**, *13*, 2381–2390. [CrossRef]
27. Chen, P.; Zhang, Q.; Su, Y.; Shen, L.; Wang, F.; Liu, H.; Liu, Y.; Cai, Z.; Lv, W.; Liu, G. Accelerated photocatalytic degradation of diclofenac by a novel CQDs/BiOCOOH hybrid material under visible-light irradiation: Dechloridation, detoxicity, and a new superoxide radical model study. *Chem. Eng. J.* **2018**, *332*, 737–748. [CrossRef]
28. Cui, Y.; Zhang, X.; Zhang, H.; Cheng, Q.; Cheng, X. Construction of BiOCOOH/g-C_3N_4 composite photocatalyst and its enhanced visible light photocatalytic degradation of amido black 10B. *Sep. Purif. Technol.* **2019**, *210*, 125–134. [CrossRef]
29. Li, S.; Chen, J.; Liu, Y.; Xu, K.; Liu, J. In situ anion exchange strategy to construct flower-like BiOCl/BiOCOOH p-n heterojunctions for efficiently photocatalytic removal of aqueous toxic pollutants under solar irradiation. *J. Alloys Compd.* **2019**, *781*, 582–588. [CrossRef]
30. Li, S.; Chen, J.; Jiang, W.; Liu, Y.; Ge, Y.; Liu, J. Facile construction of flower-like bismuth oxybromide/bismuth oxide formate p-n heterojunctions with significantly enhanced photocatalytic performance under visible light. *J. Colloid Interface Sci.* **2019**, *548*, 12–19. [CrossRef]
31. Li, S.; Mo, L.; Liu, Y.; Zhang, H.; Ge, Y.; Zhou, Y. Ag_2CO_3 decorating BiOCOOH microspheres with enhanced full-spectrum photocatalytic activity for the degradation of toxic pollutants. *Nanomaterials* **2018**, *8*, 914. [CrossRef] [PubMed]
32. Bajorowicz, B.; Kobylański, M.P.; Gołąbiewska, A.; Nadolna, J.; Zaleska-Medynska, A.; Malankowska, A. Quantum dot-decorated semiconductor micro- and nanoparticles: A review of their synthesis, characterization and application in photocatalysis. *Adv. Colloid Interface Sci.* **2018**, *256*, 352–372. [CrossRef] [PubMed]
33. Ouyang, S.; Li, Z.; Ouyang, Z.; Yu, T.; Ye, J.; Zou, Z. Correlation of crystal structures, electronic structures, and photocatalytic properties in a series of Ag-based oxides: $AgAlO_2$, $AgCrO_2$, and Ag_2CrO_4. *J. Phys. Chem. C* **2008**, *112*, 3134–3141. [CrossRef]
34. Zou, X.; Dong, Y.; Li, S.; Ke, J.; Cui, Y. Facile anion exchange to construct uniform AgX (X = Cl, Br, I)/Ag_2CrO_4 NR hybrids for efficient visible light driven photocatalytic activity. *Sol. Energy* **2018**, *169*, 392–400. [CrossRef]
35. Xu, D.; Cheng, B.; Wang, W.; Jiang, C.; Yu, J. Ag_2CrO_4/g-C_3N_4/graphene oxide ternary nanocomposite Z-scheme photocatalyst with enhanced CO_2 reduction activity. *Appl. Catal. B* **2018**, *231*, 368–380. [CrossRef]
36. Wu, X.-F.; Sun, Y.; Li, H.; Wang, Y.-J.; Zhang, C.-X.; Zhang, J.-R.; Su, J.-Z.; Wang, Y.-W.; Zhang, Y.; Wang, C.; et al. In-situ synthesis of novel p-n heterojunction of Ag_2CrO_4-$Bi_2Sn_2O_7$ hybrids for visible-light-driven photocatalysis. *J. Alloys Compd.* **2018**, *740*, 1197–1203. [CrossRef]
37. Azami, M.; Haghighi, M.; Allahyari, S. Sono-precipitation of Ag_2CrO_4-C composite enhanced by carbon-based materials (AC, GO, CNT and C_3N_4) and its activity in photocatalytic degradation of acid orange 7 in water. *Ultrason. Sonochem.* **2018**, *40*, 505–516. [CrossRef]
38. Kushwaha, A.K.; Ugur, S.; Akbudak, S.; Ugur, G. Investigation of structural, elastic, electronic, optical and vibrational properties of silver chromate spinels: Normal ($CrAg_2O_4$) and inverse (Ag_2CrO_4). *J. Alloys Compd.* **2017**, *704*, 101–108. [CrossRef]

39. Gong, Y.; Quan, X.; Yu, H.; Chen, S. Synthesis of Z-scheme Ag_2CrO_4/Ag/g-C_3N_4 composite with enhanced visible-light photocatalytic activity for 2,4-dichlorophenol degradation. *Appl. Catal. B* **2017**, *219*, 439–449. [CrossRef]
40. Li, X.; Xiong, J.; Xu, Y.; Feng, Z.; Huang, J. Defect-assisted surface modification enhances the visible light photocatalytic performance of g-C_3N_4@C-TiO_2 direct Z-scheme heterojunction. *Chin. J. Catal.* **2019**, *40*, 424–443. [CrossRef]
41. Pei, L.; Li, T.; Yuan, Y.; Yang, T.; Zhong, J.; Ji, Z.; Yan, S.; Zou, Z. Schottky junction effect enhanced plasmonic photocatalysis by TaON@Ni NP heterostructures. *Chem. Commun.* **2019**, *55*, 11754–11757. [CrossRef] [PubMed]
42. Wen, X.-J.; Niu, C.-G.; Huang, D.-W.; Zhang, L.; Liang, C.; Zeng, G.-M. Study of the photocatalytic degradation pathway of norfloxacin and mineralization activity using a novel ternary Ag/AgCl-CeO_2 photocatalyst. *J. Catal.* **2017**, *355*, 73–86. [CrossRef]
43. Zhang, M.; Qi, Y.; Zhang, Z. AgBr/BiOBr Nano-Heterostructure-Decorated Polyacrylonitrile Nanofibers: A Recyclable High-Performance Photocatalyst for Dye Degradation under Visible-Light Irradiation. *Polymers* **2019**, *11*, 1718. [CrossRef] [PubMed]
44. Li, S.; Hu, S.; Jiang, W.; Zhang, J.; Xu, K.; Wang, Z. In situ construction of WO_3 nanoparticles decorated Bi_2MoO_6 microspheres for boosting photocatalytic degradation of refractory pollutants. *J. Colloid Interface Sci.* **2019**, *556*, 335–344. [CrossRef]
45. Li, X.; Fang, S.; Ge, L.; Han, C.; Qiu, P.; Liu, W. Synthesis of flower-like Ag/AgCl-Bi_2MoO_6 plasmonic photocatalysts with enhanced visible-light photocatalytic performance. *Appl. Catal. B* **2015**, *176–177*, 62–69. [CrossRef]
46. Asadzadeh-Khaneghah, S.; Habibi-Yangjeh, A.; Abedi, M. Decoration of carbon dots and AgCl over g-C_3N_4 nanosheets: Novel photocatalysts with substantially improved activity under visible light. *Sep. Purif. Technol.* **2018**, *199*, 64–77. [CrossRef]
47. Zheng, J.; Zhou, H.; Zou, Y.; Wang, R.; Lyu, Y.; Wang, S. Efficiency and stability of narrow-gap semiconductor-based photoelectrodes. *Energy Environ. Sci.* **2019**, *12*, 2345–2374. [CrossRef]
48. Liu, Z.; Leow, W.R.; Chen, X. Bio-inspired plasmonic photocatalysts. *Small Methods* **2019**, *3*, 1800295. [CrossRef]
49. Shen, X.; Zhang, Y.; Duoerkun, G.; Shi, Z.; Liu, J.; Chen, Z.; Wong, P.K.; Zhang, L. Vis-NIR light-responsive photocatalytic activity of C_3N_4-Ag-Ag_2O heterojunction-decorated carbon-fiber cloth as efficient filter-membrane-shaped photocatalyst. *ChemCatChem* **2019**, *11*, 1362–1373. [CrossRef]
50. Duan, F.; Zheng, Y.; Liu, L.; Chen, M.Q.; Xie, Y. Synthesis and photocatalytic behaviour of 3D flowerlike bismuth oxide formate architectures. *Mater. Lett.* **2010**, *64*, 1566–1569. [CrossRef]
51. Li, S.; Hu, S.; Zhang, J.; Jiang, W.; Liu, J. Facile synthesis of Fe_2O_3 nanoparticles anchored on Bi_2MoO_6 microflowers with improved visible light photocatalytic activity. *J. Colloid Interface Sci.* **2017**, *497*, 93–101. [CrossRef] [PubMed]